PERGAMON

Journal of Atmospheric and Solar-Terrestrial Physics 65 (2003) 1053–1070

Journal of ATMOSPHERIC AND SOLAR-TERRESTRIAL PHYSICS

www.elsevier.com/locate/jastp

The DTM-2000 empirical thermosphere model with new data assimilation and constraints at lower boundary: accuracy and properties

S. Bruinsma[a,*], G. Thuillier[b], F. Barlier[c]

[a] *CNES, Department of Terrestrial and Planetary Geodesy, 18 Avenue E. Belin, 31401 Toulouse Cedex 4, France*
[b] *Service d'Aeronomie, Bp 3, 91371 Verrières-le-Buisson, France*
[c] *Observatoire de la Côte d'Azur, Department CERGA, Avenue Copernic, 06130 Grasse, France*

Received 6 January 2003; received in revised form 29 April 2003; accepted 8 May 2003

Abstract

The drag temperature model (DTM) is a semi-empirical model describing the temperature, density and composition of the Earth's thermosphere. Its first version (Ann. Geophys. 34 (1978) 9) used direct measurements of exospheric temperature and atmospheric densities derived from satellite drag data. It has later been refined (J. Geodesy 72 (1998) 161). However, both models have their lower boundaries at 120 km, which are not constrained by observations. Consequently in the lower thermosphere, the modelled temperature and density structure is uncertain. For predicting satellite orbits in the lower thermosphere, more realistic density models are required. We present a new DTM model having the following improvements:

(a) Temperature and its gradient at 120 km are represented in agreement with theory and observation, using incoherent scatter radar and satellite-borne interferometer data.
(b) Atmosphere explorer (AE) data, which have not been assimilated in DTM-94, are used as they cover a complete solar activity cycle.
(c) The Mg II index is used whenever possible to represent the solar UV and EUV emission intensity instead of the solar decimetre radio flux, since it is more representative of solar instantaneous chromospheric activity than $F_{10.7}$ is.

The basic DTM mathematical representation of temperature and composition is used, with, however, some additions and modifications to take into account the variations at 120 km altitude.

The temperature modelling accuracy has improved by 5–8%, and there is no model bias as a function of solar activity. The oxygen and helium modelling has improved as well, and this is demonstrated by the estimated drag scale coefficients issued from precise orbit computation. The scaling coefficients estimated using DTM-2000 are systematically closer to unity than those resulting from employing DTM-94 and MSIS-86 in the orbit computation. The minor constituents (O_2 and H) modelling is unchanged. The molecular nitrogen modelling is not improved, but this is, at least partly, caused by the poor data quality.

Despite these improvements, semi-empirical thermosphere models still suffer of weaknesses. First, they assume a steady-state equilibrium which is not necessarily reached in any circumstances. Second, the basic process of atmospheric heating by EUV is assumed to be represented by some indices (Mg II, $F_{10.7}$), while particle precipitation is represented by an index associated to a latitude without a longitude effect (K_p), although winds that transport energy suggest this effect. Third, the data accuracy and their incomplete geographical and temporal coverage are significant sources of uncertainty. Assimilation of a long time series of data, with a complete geographical coverage, and using the Mg II index will probably

*Corresponding author. Fax: +33-561253098.
E-mail addresses: sean.bruinsma@cnes.fr (S. Bruinsma).

1364-6826/03/$ - see front matter
doi:10.1016/S1364-6826(03)00137-8

increase model accuracy from the present-day RMS of 19% to 10–15%. The complete CHAMP accelerometer data set may allow the achievement of that goal after 5 years of operations in 2005.

Keywords: Density modelling; Temperature modelling; Satellite drag; Orbit determination

1. Introduction

1.1. Model purpose and weakness

Atmospheric density models are, besides their use in atmospheric studies, required to compute the atmospheric drag force in satellite orbit determination. They represent temperature and density as a function of altitude, latitude, local solar time, day of year, and parameters related to the state of atmospheric heating.

The accuracy of the model that is most used in precise orbit computations, DTM-94 (Berger et al., 1998), is about 20% (1σ) for its predicted total densities. The MSIS-86 model (Hedin, 1987) has comparable accuracy. DTM-94 is an improvement over the first Drag Temperature Model, DTM-78 (Barlier et al., 1978), which is not representative of low solar activity conditions due to the data set used in this model. This causes uncertain predictions under those conditions.

The inaccurate representation of temperature and density in the 120–220 km altitude range is due to the sparseness of data in this domain. The two basic reasons for the lower atmosphere modelling uncertainties are: first, the modelled density in the lower thermosphere results of adjustment of the model parameters at higher altitudes (220–1000 km), which have been propagated downward by means of a modified Bates temperature profile (Bates, 1959); secondly, the modelling of the temperature and its gradient at 120 km as constant values in DTM-94 causes uncertainties in the predicted density of the lower thermosphere, since significant temperature variability at that altitude is known from incoherent scatter radar observations (Alcaydé et al., 1974). However, this being acknowledged, the absence of precise data as well as data having enough spatial coverage, has lead to prefer constant boundary conditions.

This is why it is in this region that a special effort has been made to improve the modelling.

1.2. New model inputs

In this study, the temperature at 120 km (T_{120}) is modelled using incoherent scatter radar observations. The latitudinal coverage is achieved by means of three incoherent scatter radar stations namely St. Santin (45°N), Arecibo (18°N) and the European Incoherent SCATter (EISCAT), which is at approximately 70°N, and is the only available data source at that latitude.

The WIND Imaging Interferometer (WINDII) is an instrument (Shepherd et al., 1993) placed onboard the Upper Atmosphere Research Satellite (UARS), which measured temperature and wind in the lower thermosphere. WINDII data are used to determine the vertical temperature gradients ($\mathrm{d}T_{120}$) as a function of local time, latitude and season. They have also been used to derive relative density variations at 120 km altitude (Bruinsma et al., 2002). The variations derived in that study are taken into account in DTM-2000.

Data from the Atmosphere Explorer-C and -E satellites (NSSDC CD-ROM) are assimilated in order to better reproduce in particular the temperature under low solar activity conditions.

The Mg II index (Heath and Schlesinger, 1986) is used as a proxy indicator to represent the solar activity in the EUV and UV whenever possible, which is to say, for data after 1978. Before that date, the solar radio flux at 10.7 cm ($F_{10.7}$) is used. It has recently been demonstrated (Thuillier and Bruinsma, 2001) that the Mg II index is more representative of the solar radiation that governs upper atmosphere heating processes than $F_{10.7}$ is, while these indices are nearly 100% correlated over periods of at least several years. It is this property that enables both Mg II and $F_{10.7}$ to be used in the model adjustments.

The next section reviews the data used in this study, and presents the data processing that allowed the modelling of T_{120} and $\mathrm{d}T_{120}$. The DTM algorithms and the additional temperature and density variations (with respect to variations already represented in DTM-94) are described in Section 3. The results are presented in Section 4 which includes comparisons with DTM-94 and MSIS-86. The various results, the limiting factors in empirical modelling, the effects of data availability, and distribution and accuracy of the estimations, are discussed in Section 5. The future model improvements expected by new and consistent data are presented in Section 6.

2. Data and external modelling results

The following subsections describe the incoherent scatter radar and WINDII data used in the temperature and temperature gradient modelling at 120 km, respectively. They are modelled in spherical harmonics and are introduced in the DTM algorithm described in Section 3. The third subsection gives a short description of relative density variations at

120 km, derived from tidal wind measurements. Section 2.4 reviews the accuracy and geographical and temporal coverage of the temperature and density data used to re-estimate the DTM model coefficients. This section ends with a short description of the Mg II index.

2.1. Modelling of dT_{120}

One type of observation provided by WINDII is the kinetic temperature that is derived from the measured Doppler width of the atomic oxygen green line emission (557.7 nm). The vertical temperature gradient at 120 km altitude is calculated by modelling the temperature above and below this altitude, and taking the difference and dividing by the height interval. These data cover -70° to 70° latitude over a period of 4 years (1992–1996). However, they do not allow the determination of solar activity dependent variations. The absolute values of the temperature observations are erroneous because of calibration and instrumental uncertainties. WINDII observes the green line intensity simultaneously in the altitude range 87–200 km, and it is therefore acceptable to assume that the same bias affects consecutive altitude levels allowing to derive the temperature gradient, but unfortunately not the temperature at 120 km.

Temperature and wind in the lower thermosphere have a tidal structure due to their origin. The noise in the measurements necessitates an averaging procedure to extract a tidal signal. A simple binning technique may be used because the aliasing of the mean temperature into the tides is negligible (McLandress et al., 1996). To that purpose, the data are organized in zonal bands of 10° latitude and subsequently averaged in bins of 1 h local time. To increase the number of observations per bin and further reduce the noise, we assume identical responses of the atmosphere in each hemisphere with respect to season, so assuming a symmetrical variation. Based on solar declination, three seasons are adopted here: local summer, local winter, and equinox. The Northern Hemisphere summer is in the day-of-year interval 101–242, and its winter in the interval 0–59 and >285. Equinox conditions, in which the rapid transition from summer to winter regime or vice versa takes place, are assumed in the following intervals: between days 60–100, and between days 243–285.

The temperature observations at the altitudes 117, 120 and 125 km are rejected under the following conditions:

- moderate to high geomagnetic activity: $K_p > 4$,
- $T < 250$ K or $T > 650$ K,
- $\sigma(T) > 100$ K,
- σ (emission rate) $> 10\%$,
- emission rate < 40 photons/cm^3/s.

The first condition is to prevent the masking of the tidal signal by particle precipitation (Fesen et al., 1991). All remaining conditions were determined by analysis of the data, and eliminate the obvious outliers.

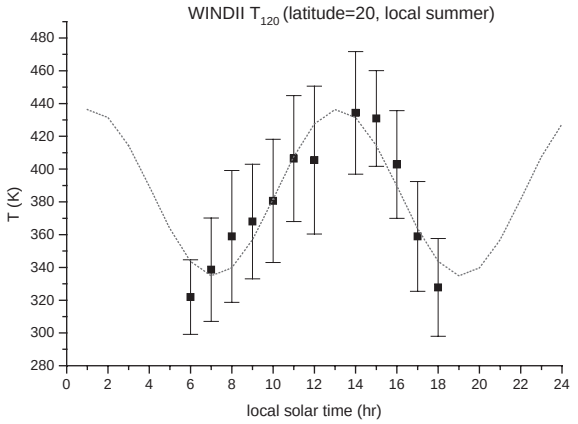

Fig. 1. Estimated semi-diurnal tidal signal (dotted line) and the averaged WINDII temperature observations and corresponding 1σ uncertainty.

A tidal signal $S(t)$ of the following form is extracted from the averaged observations, per zonal band of 10°N latitude and for the three altitude levels, by least-squares adjustment:

$$S(t) = A\cos\frac{2\pi}{24}(t-\phi_1) + B\cos\frac{2\pi}{12}(t-\phi_2) + C, \qquad (1)$$

where A and B, and ϕ_1 and ϕ_2 are the diurnal and semi-diurnal tide amplitudes and phases (time of maximum), respectively, C the mean tidal signal, and t the solar local time in hours. The most complete local time coverage occurs in the 90–110 km altitude range between -40° and 40° latitude. At 120 km, the green line is only observable during the day. This means that for the winter hemisphere the local time coverage is only 8–11 h, while it is 11–17 h for the summer hemisphere. Based on analysis of WINDII and radar data, and predictions from the numerical Global Scale Wave Model (GSWM; Hagan et al., 1995), it was established that the diurnal tide is almost an order of magnitude smaller than the semi-diurnal tide in the 117–125 km altitude interval and from -60° to 60° latitude. Therefore, it was decided to only estimate the semi-diurnal and constant tidal components. Being closer to the source of energy deposition, the diurnal tide becomes dominant for altitudes exceeding 150–160 km. Fig. 1 shows an example of the estimated semi-diurnal tidal signal at 120 km fitted to the averaged observations for 20° latitude and local summer. The uncertainty of the averaged observations represents the computed standard deviations per bin, which is 40 K on average despite the averaging and data selection.

Incoherent scatter radar temperature observations consist of ion and not neutral temperatures. These temperatures are equivalent when the geomagnetic activity and the electric field strength are small, so when the Joule heating and particle precipitation effects are negligible (Banks and Kockarts, 1973). The EISCAT observations are binned following the

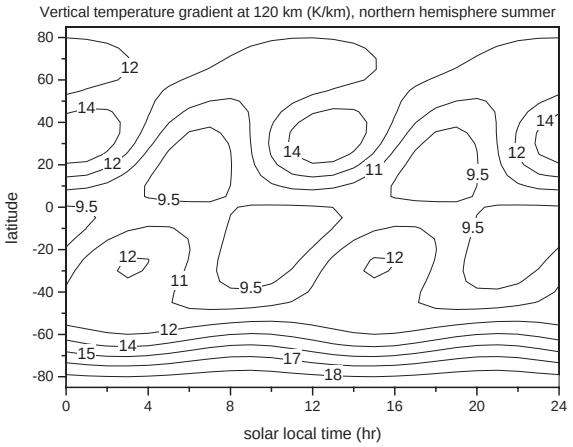

Fig. 2. Vertical temperature gradient model derived from WINDII and EISCAT observations.

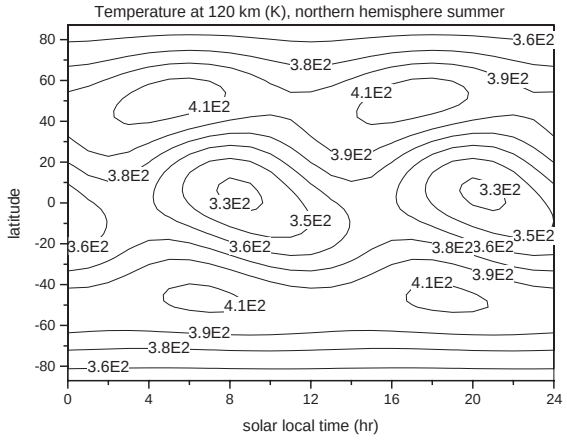

Fig. 3. Temperature at 120 km altitude model derived from EISCAT, St. Santin and Arecibo observations.

procedure described for the WINDII data, but the data selection criteria are more severe because of its location in the auroral zone where particle precipitations are frequent and prevent a correct estimate of neutral atmosphere parameters (e.g. the temperature) from the ionospheric data. Only observations under weak to moderate solar activity conditions ($F_{10.7} < 130$), comparable to the WINDII data conditions, are used. The gradients from EISCAT data are derived using the estimated temperatures at 117 and 123 km. The dT_{120} model is obtained using WINDII derived gradients up to $|60^\circ|$ from the altitude difference (125–117 km). We have verified that they agree within uncertainty (better than 2.5 K/km) with the St. Santin and Arecibo incoherent scatter radars measurements. The WINDII and EISCAT derived gradients data are represented by spherical harmonics of degree and order up to 6 using a least-squares adjustment. We verified that coefficients of order greater than 2 are close to zero given the semi-diurnal nature of the data. This provides a global representation of the temperature gradients, however without observations above 70° to constrain the calculation. Fig. 2 presents the modelled gradients (with an uncertainty of 2.5 K/km) for summer on the Northern Hemisphere. The winter representation is obtained by symmetry about the equator. The constant DTM-94 gradient of 14.35 K/km is larger than the mean value of this model (13.8 K/km), while local differences are up to 40%.

2.2. Modelling of T_{120}

Following the WINDII data reduction procedure described in the last subsection, the semi-diurnal tidal components are estimated using averaged temperature data from the three incoherent scatter radar stations, EISCAT (70°N), St. Santin (45°N) and Arecibo (18°N). Data are available mainly during low solar activity, and few under moderate solar activity. Variations due to the solar cycle cannot be properly estimated with these observations. Moreover, St. Santin and Arecibo are located at lower geomagnetic latitudes where direct particle precipitations and Joule heating effects are negligible. Therefore, the selection criteria applied to the data of these stations, do not reject many observations since the electric field amplitude condition is generally met. The summer, winter and equinox seasons are in accordance with the definitions given in the previous subsection, and symmetrical seasonal response of the atmosphere is assumed. The resulting data given for three latitudes per hemisphere, are used in a least-squares procedure to obtain spherical harmonic coefficients up to degree and order 6 and thus a continuous representation up to the poles by extrapolation. Fig. 3 presents the modelled temperatures at 120 km for summer in the northern hemisphere. As for the case for Fig. 2, the winter representation is obtained by symmetry about the equator. DTM-94's globally constant value for T_{120} of 380 K is equal to the mean value of T_{120} in DTM-2000.

2.3. Relative density variations at 120 km

The tidal wind observations at 120 km altitude of the instrument WINDII have been used to derive the relative density variations in accordance with tidal theory (Bruinsma et al., 2002). The data from February 1992 through August 1996 were used from 60°S to 60°N latitude, while averaging was achieved by processing the data in both 2-month and latitudinal bins in a way similar to the data reduction procedure described in Section 2.1. The results are geographical distributions of the relative density variations every 2 months (January + February, March + April, etc.), an example of which is given in Fig. 4 for the average variation in the months July and August. Comparison with Fig. 3, which shows the modelled temperature at 120 km, shows that the amplitude and phase of the variations are in agreement, but

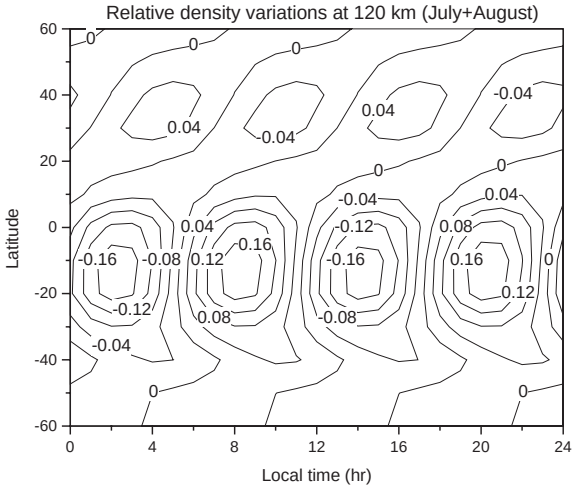

Fig. 4. WINDII-derived average relative density variations (density variation over mean density ratio) at 120 km for the months July and August.

that there is an offset between the maxima of approximately 10°. For latitudes higher than 60°S and 60°N, no information is available. Consequently, in the polar regions, the relative density variation is extrapolated. However, at the EISCAT latitude, in low to moderate geomagnetic activity, the temperature pattern is nearly constant (Fig. 3), supporting (partly) the extrapolation imposed by lack of pertinent information in these polar regions.

2.4. Assimilated temperature and density data

The Dynamics Explorer 2 (DE-2) Neutral Atmosphere Composition Spectrometer (NACS; Carignan et al., 1981) and Wind And Temperature Spectrometer (WATS; Spencer et al., 1981) data sets, were assimilated in DTM-94, and are also in DTM-2000. Furthermore, the Atmosphere Explorer (AE-C and AE-E) data from the Neutral Atmosphere TEmperature instrument (NATE; Spencer et al., 1973), the Neutral Atmosphere Composition Experiment (NACE; Pelz et al., 1973), and the Open Source Spectrometer (OSS; Nier et al., 1973) are also assimilated in DTM-2000. Their precisions are functions of altitude and solar activity. The AE-E NATE temperature observations are important, because they constitute the only available consistent single-instrument data set covering the complete solar activity range. Table 1 presents the data sets and their geographical coverage, as well as their precision or accuracy. Because the data sets marked with an asterisk are affected by systematic bias besides the random uncertainties, the accuracy cannot be given. The data sets are plotted as a function of time, and thus solar activity, in Fig. 5.

The Atmosphere Explorer data used in this study have been selected in the intervals given in Fig. 5 which shows the entire temporal coverage. This is caused by the elimination of many observations due to poor precision during certain periods of the mission. The AE-E MESA (Miniature ElectroStatic Accelerometer) total density data were not assimilated in the DTM-2000 model because of their limited spatial and temporal coverage; however, they are used as validation data in Section 4.3.

Table 1
The temperature, partial and total density data sets assimilated in DTM-2000

Data set	Data type	Altitude (km)	Latitude (deg)	Precision
OGO-6	T	230–270	−90; 90	65 K[a]
DE-2 WATS	T	225–600	−90; 90	50 K
AE-E NATE	T	140–400	−20; 20	50 K
Radar	T	100–150	18N; 48N; 70N	40 K
WINDII	T	117–125	−65; 65	40 K
DE-2 NACS[b]	He	400–1000	−90; 90	1–3%
AE-E NACE[b]	He	300–600	−20; 20	2–10%
DE-2 NACS[b]	O	275–575	−90; 90	1–5%
AE-C OSS	O	300–400	−68; 68	20%[b]
AE-E NACE[b]	O	300–475	−20; 20	2–10%
DE-2 NACS[b]	N_2	225–400	−90; 90	1–5%
AE-E NACE[b]	N_2	140–250	−20; 20	2–10%
DTM database[b]	ρ	225–1000	−90; 90	5–15%
CACTUS (Villain, 1980)	ρ	225–500	−30; 30	2–8%
AE-C MESA[b]	ρ	140–300	−68; 68	5–15%

[a] Absolute precision.
[b] Calibration problems and/or data inconsistencies.

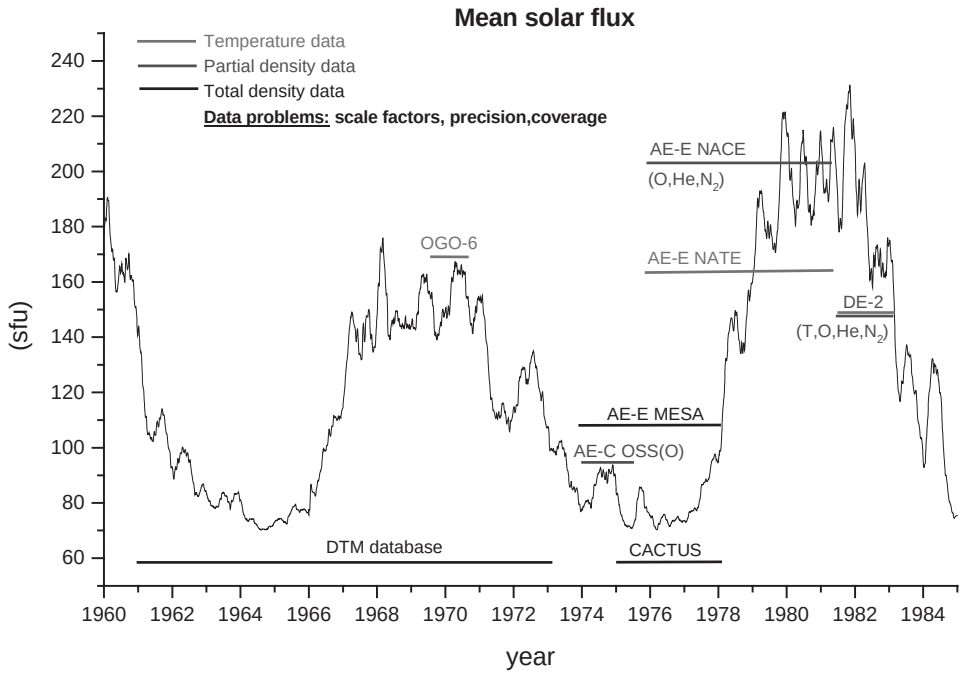

Fig. 5. Temperature, total and partial density data sets as a function of the 10.7 cm solar flux.

2.5. The Mg II index

A synthesis of the results and the conclusion presented by Thuillier and Bruinsma (2001) regarding the Mg II index, derived from satellite-borne Sun spectrometer observations, are given next for reasons of convenience.

The EUV radiation that heats the terrestrial atmosphere originates in several distinct layers of the Sun: the chromosphere, transition region and corona while the radio flux at 10.7 cm originates in the high chromosphere/lower corona of the solar atmosphere (Thuillier and Bruinsma, 2001). This is why looking for an EUV variability proxy indicator is not a straightforward task. Calculating averaged values over 3 solar rotations, the mean radio flux is correlated with the mean EUV radiation (up to 0.99) while the correlation is weaker between the daily values (approximately 0.88) (Hedin, 1984).

The Mg II index was proposed by Heath and Schlesinger (1986), and is computed as the irradiance ratio of the Mg II chromospheric core emission at 280 nm to the line wings continuum. The correlation of the Mg II index with specific EUV emissions is better than that of $F_{10.7}$ for short term time scales, typically the solar rotation. However, $F_{10.7}$ is frequently used in atmospheric modelling because of its continuous time series obtained by the National Research Council of Canada since 1947.

The index used in this study, corrected for instrumental slit function (Cebula et al., 1998), is derived from several instruments onboard satellites from the National Oceanic and Atmospheric Administration (NOAA). The Mg II data span November 1978 through October 1997. They have been scaled to $F_{10.7}$ units (Thuillier and Bruinsma, 2001) so that both indices can be used in the density model. The correlation between Mg II and $F_{10.7}$ is 0.99 over the entire data set of 19 years. However, a RMS difference of approximately 12% exists for periods of the order of months due to the different behaviour of these emissions at short time scales.

Comparison by means of test models demonstrated the better representativity of the Mg II index with respect to upper atmosphere heating processes compared to $F_{10.7}$. This conclusion is based on smaller standard deviations of the DE-2 residuals and better orbit fits using Mg II. The fact that the density model based on Mg II is more accurate than that based on $F_{10.7}$ under high solar activity, where these proxies differ most, demonstrates the higher representativity of the Mg II index of upper atmosphere heating processes. The Mg II index is only concurrent with the DE-2 data, all other data sets being prior to 1978.

2.6. Calibration of the data

Calibration of the mass spectrometer data, the DE-2 NACS and AE-E NACE data in particular, is required because the instruments have not been (could not be) calibrated under laboratory conditions. The principle of determining the instrumental responsivity (calibration parameters), scale factors in this case, consists in comparing

the mass spectrometer observations to total density measurements that are derived from satellite drag.

Hedin (1987) and Berger et al. (1998) estimated the DE-2 NACS scale factors (one per constituent), which are given in Table 4. For MSIS-86, the model parameters and scales factors were simultaneously determined by fitting to all the data. Therefore, the calibration of the NACS data is based on all other data used in the model. In case of DTM-94, a preliminary model using total density measurements obtained from satellite drag and CACTUS data was developed, but it was valid only for low to moderate solar and geomagnetic activity (mean flux less than 170, and K_p less than 4) given the time coverage of the data. Then, NACS data corresponding to the same solar previous conditions have been compared to this model predictions to obtain the scale factors. Afterward, it was assumed that the so-obtained scale factors were valid for the entire DE-2 mission.

The MSIS-86 and DTM-94 values agree within 5% except for the molecular nitrogen scale factor (0.7 vs. 0.6) despite the different estimation procedures employed. The 1σ uncertainty of the DTM-94 estimations ranges from 26% to 37% (MSIS-86 uncertainties are not given). These results are satisfactory taking the number of data that are comparable with respect to altitude, latitude, local time and geomagnetic activity into account: the total density data sets (last frame of Table 1) only cover the same solar activity interval as the DE-2 NACS data sets over a period of 5 months.

A different approach is used in this study to determine the mass spectrometer scale factors. Precise orbit determination (POD), using accurate satellite tracking data and force models for the gravitation, and the direct and indirect solar radiation pressure effect on the spacecraft, can provide information for the spectrometer calibration. Thanks to the tracking data, the atmospheric density model prediction can on average be corrected for over the duration of the arc through the estimation of drag scale factors (Berger et al., 1998). This means that, over the duration of the arc, accurate mean density values are determined. A density model is unbiased if the estimated drag scale factors are unity (on average), which number is obtained when a model for the drag coefficient is used (Cook, 1965). By choosing satellites (altitudes) and epochs (solar activity) judiciously, one can obtain information mainly on a single atmospheric constituent. The geodetic satellites Starlette and Stella, at approximately 800 km altitude, and GFZ-1 at 380 km, with orbital inclinations of 50°, 97° and 51°, respectively, and small eccentricities (smaller than 0.02) are used in this study. Their spherical shapes avoid attitude related orbit uncertainties, and provide the best possible accuracy of approximately 5% for the drag coefficients (Gaposhkin and Coster, 1994). Their individual satellite trajectories are each time fitted to 7 days of Satellite Laser Ranging (SLR) data in case of Starlette and Stella, and 4 days of SLR data in case of GFZ-1. Drag scale factors are estimated on a daily basis, which is sufficient to determine a constant density model scale offset such as caused by the assimilation of uncalibrated mass spectrometer data. The epochs correspond to solar minimum (1996–1997; 16 days of GFZ-1 and 35 days of Stella) and solar maximum (1991–1992; 70 days of Starlette) conditions. Starlette and Stella evolve in an atmosphere composed of 80–90% oxygen and 10–20% helium during high solar activity, while atmospheric composition is more than 95% helium during low activity. At GFZ-1's altitude, the atmosphere consists of approximately 85% oxygen and 15% molecular nitrogen. These satellites were used to calibrate the DE-2 oxygen data by simultaneously estimating model coefficients, mass spectrometer scale factors and density scale factors. The DE-2 scaling factor of 0.79, resulting in the least-biased drag scale factor estimations in the POD, was applied in this study. The AE-E NACE oxygen data scale factor of 0.89 was determined in a similar way.

The direct calibration of the DE-2 helium data is impossible, because accurate estimation of drag scale factors for satellites at 1000–1500 km altitude (i.e. where helium is the major constituent under high solar activity) is not possible due to the radiation pressure forces, which are approximately one to two orders of magnitude larger than the drag force. Secondly, an adequate geodetic spacecraft is not in orbit in that altitude range. Similarly, due to the absence of total density data in the 120–150 km altitude interval where N_2 is the major constituent, direct calibration of the DE-2 N_2 data is equally impossible. Thus, the scale factors for these constituents were determined indirectly as in MSIS-86 through the simultaneous estimation of scaling parameters in the data fitting procedure.

3. The DTM-2000 algorithm

The representation of the total density in the altitude range 120–1500 km is achieved by summing the contributions of the main thermospheric constituents (N_2, O_2, O, He, H), under the hypothesis of independent static diffuse equilibrium (which is not always attained (Aikin et al., 1993; Hedin, 1989), but its effect on density is presently not taken into account). The height function $f_i(z)$ per constituent i is the result of the integration of the differential equation of diffusive equilibrium:

$$f_i(z) = \left(\frac{T_{120}}{T(z)}\right)^{1+\alpha+\gamma_i} \exp(-\sigma\gamma_i\zeta), \tag{2}$$

with $T(z) = T_\infty - (T_\infty - T_{120})\exp(-\sigma\zeta)$, T_∞ is the exospheric temperature, α the thermal diffusion coefficient for He and H (-0.38), $\gamma_i = m_i g(120\text{ km})/(\sigma k T_\infty)$, m_i the atomic or molecular mass, $g(120\text{ km})$ = gravity acceleration at 120 km altitude, σ the relative vertical temperature gradient $\mathrm{d}T_{120}/(T_\infty - T_{120})$, k the Boltzmann constant 1.3803×10^{-23} J K^{-1}, ζ the geopotential altitude $(z - 120)(R + 120)/R + z$, and R is the polar Earth radius 6356.770 km.

This function has already been described in detail by Berger et al. (1998), but it is given again here to show were T_{120} and $\mathrm{d}T_{120}$ intervene in the algorithm. Using this function, the neutral density given at 120 km altitude can be propagated to higher altitudes. The partial density variations as a function of the environmental parameters L (latitude, longitude, solar local time, solar flux, and geomagnetic activity) are reproduced by means of a spherical harmonic function $G(L)$. The total density at altitude z is then calculated as follows:

$$\rho(z) = \sum_i \rho_i(120\ \mathrm{km}) f_i(z) \exp(G_i(L)). \tag{3}$$

DTM-94 models the exospheric temperature and the atmospheric constituents each with up to 38 coefficients a_i. The spherical harmonic function G is used to describe periodic and non-periodic variations. Periodic variations are given as annual and semi-annual terms, as well as diurnal, semi-diurnal and ter-diurnal terms. These periodic terms are also a function of latitude, for which associated Legendre functions $P_{n,m}$ of degree n and order m are used. The non-periodic terms consist of constant latitude terms, and are associated with solar and geomagnetic activity. The extensions to the function G with respect to the one used in DTM-94 (thoroughly described in that paper) are given below.

Non-periodic terms:

$$\begin{aligned} &a_{77}P_{3,0} + a_{78}P_{5,0} + a_{79}P_{6,0}, \\ &a_{85}(\bar{F} - 150)P_{2,0} + a_{86}(\bar{F} - 150)P_{3,0} \\ &\quad + a_{87}(\bar{F} - 150)P_{4,0}, \\ &a_{64}\bar{K}_p + a_{65}\bar{K}_p P_{2,0} + a_{68}K_p P_{4,0}. \end{aligned} \tag{4a}$$

Semi-diurnal periodic terms:

$$\begin{aligned} &a_{88}P_{3,2}\cos 2\omega t + a_{89}P_{3,2}\sin 2\omega t \\ &\quad + a_{90}P_{5,2}\cos 2\omega t + a_{91}P_{5,2}\sin 2\omega t \\ &\quad + a_{92}P_{6,2}\cos 2\omega t + a_{93}P_{6,2}\sin 2\omega t, \end{aligned} \tag{4b}$$

where the coefficients a_i are estimated by means of least-squares adjustment for each constituent and temperature, $\bar{F}$ represents the solar flux averaged (with a moving window) over the preceding three ($F_{10.7}$) or one (Mg II) solar rotation, and $\bar{K}_\mathrm{p}$ and K_p represent the last 24-h mean and 3-h delayed 3-h planetary geomagnetic index, respectively, and ω is the Earth rotation rate. The averaging is differently made for $F_{10.7}$ and Mg II. Mg II correlates better with the EUV solar emission than $F_{10.7}$. As this occurs from time to time, the decorrelation EUV/$\mathrm{F}_{10.7}$ is decreasing when the averaging is made for more than a single solar rotation. This is supported by the nearly 100% correlation between these two indices over a few years. This was likely the reason why the 3-solar rotation averaging was made since the first models made in the 1970's.

Table 2
The (maximum) number of DTM model coefficients at the lower model boundary and for the exospheric temperature. The constituents are given at the lower model boundary only and propagated upward by means of the temperature profile

	DTM-78	DTM-94	DTM-2000
Temperature at 120 km	2	2	25
Constituents at 120 km	42	45	60
Exospheric temperature	42	45	60

The addition of latitudinal and semi-diurnal terms is required because of the external (Section 2) modelling results of T_{120} and $\mathrm{d}T_{120}$. The remaining terms are based on analysis of the residuals computed with DTM-94 and the data sets, which showed slight solar flux and geomagnetic activity signature. The algorithm has been written in a general form in order to easily accommodate future coefficients. Presently the model employs 25 coefficients for the lower boundary condition and up to 60 for the exospheric temperature and the constituents. DTM-78 and DTM-94 use up to 42 and 45 coefficients for the exospheric temperature and the constituents, respectively, while both models employ only 2 coefficients for the lower model boundary (e.g. constant values for T_{120} and $\mathrm{d}T_{120}$). Table 2 sums up the number of model coefficients employed in the DTM models.

4. Results

The adjustment of the model coefficients is done by means of a least-squares procedure; only those coefficients were retained in the solution that had a statistical uncertainty from the fit of less than a tenth of the coefficient value. The properties of the modelling are analysed by mean and RMS of the residuals, which we have defined as 'observed/calculated' (O/C). The data sets that are marked with an asterisk in Table 3 are affected by systematic uncertainties and some of them require the application of instrumental calibration factors, which are discussed in the next section. The RMS of the residuals represents a combination of the ability of the model to reproduce the observed variations and the geophysical and instrumental noise in the observations. The residuals are binned as a function of altitude, latitude, local time, month, $\bar{F} - 150$ and K_p. Analysis of the mean and RMS of the residuals may give clues about the modelling uncertainties, as well as about data inconsistencies. Specific results are presented in the following subsections.

Only the DE-2 data were processed using the Mg II index, all other data sets being prior to its observation. Those data were processed using $F_{10.7}$, and results are for that reason noisier because of its lesser representativity of the state of atmospheric heating.

Table 3
DTM-94, DTM-2000 and MSIS-86 model evaluation with respect to the selected data sets, covering low (L) or high (H) solar activity, for all geomagnetic activity levels. The mean, followed by the RMS in percent, of the residuals (O/C) is shown. The data sets marked with an asterisk are affected by systematic uncertainties and/or require the application of calibration factors

Data set		DTM-94	DTM-2000	MSIS-86
OGO-6	T (H)	0.99; 11.8	1.00; 11.8	0.99; 11.7
DE-2 WATS	T (H)	0.98; 6.3	1.00; 6.0	1.00; 6.4
AE-E NATE	T (L + H)	0.97; 6.7	1.00; 6.2	0.98; 6.2
DE-2 NACS*	He (H)	0.79; 21.9	0.63; 20.8	0.85; 18.7
AE-E NACE*	He (L + H)	0.91; 19.1	0.70; 16.1	0.93; 14.7
DE-2 NACS*	O (H)	0.87; 18.7	0.79; 16.6	0.87; 18.9
AE-C OSS	O (L)	1.01; 27.8	1.04; 26.3	1.02; 25.2
AE-E NACE*	O (H)	0.95; 18.3	0.89; 17.6	0.91; 16.9
DE-2 NACS*	N_2 (H)	0.64; 28.3	0.68; 28.5	0.56; 28.9
AE-E NACE	N_2 (L)	1.06; 26.0	1.02; 24.0	1.02; 21.8
DTM database*	ρ (L + H)	0.96; 19.2	0.99; 18.9	0.97; 18.7
CACTUS	ρ (L)	0.96; 19.3	0.98; 19.4	1.00; 19.2
AE-C MESA*	ρ (L)	1.10; 19.8	1.04; 19.4	1.12; 19.6

4.1. Temperature modelling

The global mean and RMS of the DTM-2000, DTM-94, and MSIS-86 residuals are presented in the top frame of Table 3. The improvement in modelling the temperature variations (RMS) is approximately 0.3% and 0.5% for 'DE-2 WATS T' and 'AE-E NATE T', respectively. More importantly, DTM-2000 reproduces the temperatures unbiased for the 3 data sets, especially compared to the 3% bias of DTM-94 because of the low solar activity data used in this model, and the 2% bias of MSIS-86. The total uncertainty of the temperature modelling, resulting from the uncertainties contributions to the individual model coefficients, is less than 0.0009 (0.09%). Fig. 6 shows the geographical distribution of temperature obtained with DTM-2000, DTM-94 and MSIS-86 for the altitudes 200 and 500 km (flux = mean flux = 150, day-of-year = 180, $K_p = 0$. MSIS-86, DTM-94, and DTM-2000 at 500 km altitude exhibit the same global structures. The temperature at 120 km altitude for DTM-2000 was already shown in Fig. 3. At 200 km altitude (Fig. 6a), DTM-2000 and MSIS-86 have two maxima in the summer hemisphere. DTM-94 has one maximum at about 16 h local time and from 20°S up to 90°N, and this structure basically remains the same at 500 km. The largest differences between the DTM models and MSIS-86 at 200 km are the maximum and minimum values; MSIS-86 is more than 100 K hotter in the summer hemisphere, and 50 K cooler in the winter hemisphere. At 500 km altitude (Fig. 6b), MSIS-86 still has two maxima, which have shifted by approximately 1 h (later) with respect to 200 km. DTM-2000 has one distinct maximum between 10°N to 50°N at about 17 h local time, which is also approximately 1 h later with respect to the maximum at 200 km. This maximum is 10 K hotter than the DTM-94 and 30 K cooler than the MSIS-86 maxima, respectively. The DTM-2000 minimum value is approximately 45 and 85 K hotter than the DTM-94 and MSIS-86 minima, respectively. From Figs. 6, it can be deduced that the MSIS-86 vertical temperature gradient at 200 km altitude is significantly smaller than that of both DTM models.

The exospheric temperature of DTM-2000 follows the subsolar latitude in an annual variation (not shown). In the absence of geomagnetic activity (i.e. K_p equals zero) and local summer, the maximum is at approximately 35° latitude (on the summer hemisphere) at 16:30 local solar time. DTM-94, on the other hand, predicts the maximum at approximately 20° latitude also at 16:30 local solar time, but presents a second maximum on the (summer) pole even for $K_p = 0$. For the three models, times of maximum temperature agree.

As a general remark on the quality of the modelling of the different thermospheric parameters, the temperature modelling seems more accurate than the individual constituent modelling is, as may be seen in Table 3. Moreover, the selected temperature data sets cover the entire solar activity range, which is not true for the constituent or total density data sets. The DE-2 and AE-E temperature data are unbiased with respect to the absolute OGO-6 measurements (Thuillier et al., 1977), and the three data sets seem compatible. Fig. 7 displays the means of the residuals binned as a function of solar activity between DTM-2000, DTM-94 and MSIS-86 and the AE-E and DE-2 data sets sets (OGO 6 is not shown in

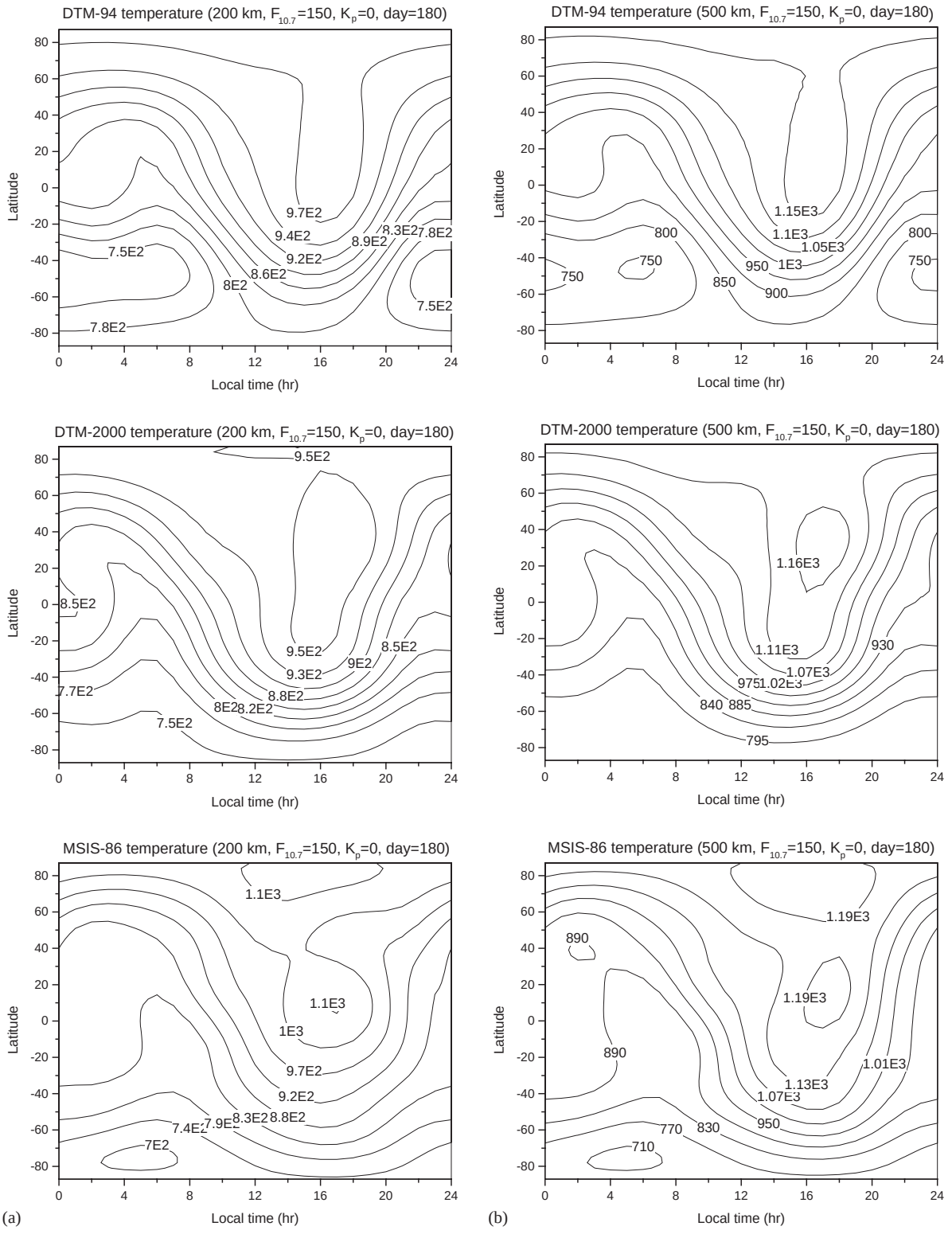

(a) (b)

Fig. 6. Geographical distribution of temperature at 200 (a) and 500 km (b) altitude, obtained with DTM-94, DTM-2000 and MSIS-86.

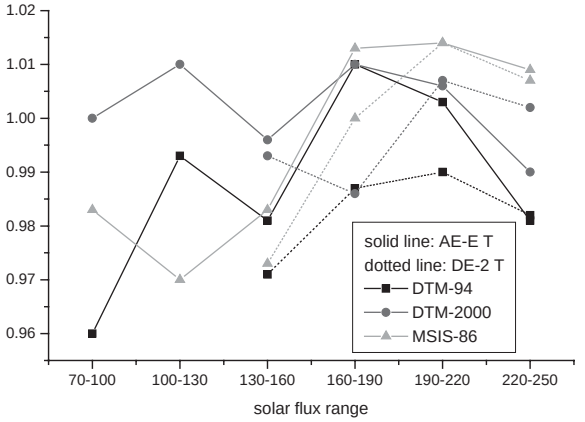

Fig. 7. Mean of the AE-E and DE-2 temperature residuals as a function of 81-day mean 10.7 cm solar flux.

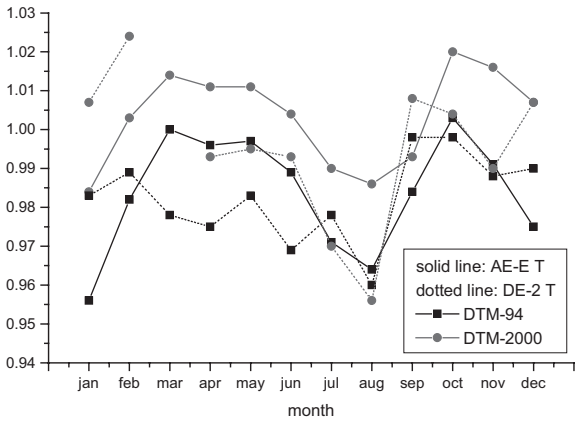

Fig. 8. Mean of the AE-E and DE-2 temperature residuals as a function of month.

Fig. 7, but it is not biased as a function of solar activity with DTM-2000). The variability as a function of solar activity is the least with DTM-2000.

Analysis of the residuals did not reveal unmodelled variations or systematic differences, with the exception of the binning as a function of month. Here, significant biases exist as is shown in Fig. 8, where the missing months (March and December) with DTM-2000 are due to data gaps in the Mg II observations. For August, all models display a large discrepancy. It is a transition month between solstice and equinox, and we have verified that it is not an artefact of the T_{120} and dT_{120} (Section 2.1). The AE-E NATE binned residuals do not present discontinuities, as do the two other data sets.

4.2. Total density modelling and orbit computation results

The total density modelling is improved, as shown in the last frame of Table 3. With respect to MESA, the bias of DTM-2000 is the smallest (4% to be compared with 10 and 12% for the two other models) A similar improvement is shown in Table 3 for the CACTUS and DTM database, however the variation of density is reproduced with an equivalent accuracy of approximately 19% by the three models. The low precision of the DTM database and MESA data sets make improvement difficult to quantify. Furthermore, the CACTUS data set contributes only to the model accuracy at low latitudes due to its latitudinal coverage. Fig. 9 shows the geographical distribution of the density obtained with DTM-2000, DTM-94 and MSIS-86 for the altitudes 120, 500 and 800 km (flux = mean flux = 70, day-of-year = 15, $K_p = 0$). The DTM-2000 densities and their local time distribution are in better agreement with MSIS-86 than DTM-94 is, notably due to more realistic modelling at the lower model boundary. However, the MSIS-86 semi-diurnal variations have their maxima 1 h later and around 10° lower than DTM-2000 (Fig. 9a). But also at higher altitudes, the latitudinal structure is in better agreement, with maxima that are closer to the subsolar latitude. However, the amplitude of the DTM-2000 maximum is larger than that of MSIS-86 at 800 km, while a reverse situation is found at 500 km (Figs. 9b and c). We also note the close behaviour of DTM-2000 and MSIS-86 at 500 km and the larger extension of the density bulge (helium) of MSIS-86 with respect to the two other models (Fig. 9c).

Fig. 10 shows the seasonal variations of DTM-2000, DTM-94 and MSIS-86 at 3 altitudes (200, 500 and 800 km) for 45°S and 45°N (flux = mean flux = 150, local time = 14 h, $K_p = 0$). The semi-annual variation is present at all altitudes, but the peak-to-peak amplitudes of DTM-94 of the second maximum (around day-of-year 310) in the Northern Hemisphere in particular are up to 25% larger than of both other models. These differences can in part be explained by the use of different time-periods of the datasets since the semi-annual variation varies from year to year. At 200 km altitude, DTM-2000 predicts an up to 25% higher density for the months December and January. The AE-C MESA total density data (Table 3), binned for those 2 months, indicate that DTM-2000 indeed over-estimates density between 140 and 250 km, but by less than 7%. The minima of the three models (around day-of-year 200) agree best at 500 km and are within 2 weeks of each other at 200 and 800 km; however, the amplitude of DTM-94 at 45°N, and 200 km is around 20% larger than for DTM-2000 and MSIS-86. The disagreement between the models is largest at 200 km altitude because of the lack of low-altitude data assimilated in the models. At that altitude, the partial molecular nitrogen and atomic oxygen densities are nearly equal. The months November through February are restituted with an up to 20% higher density with DTM-2000,

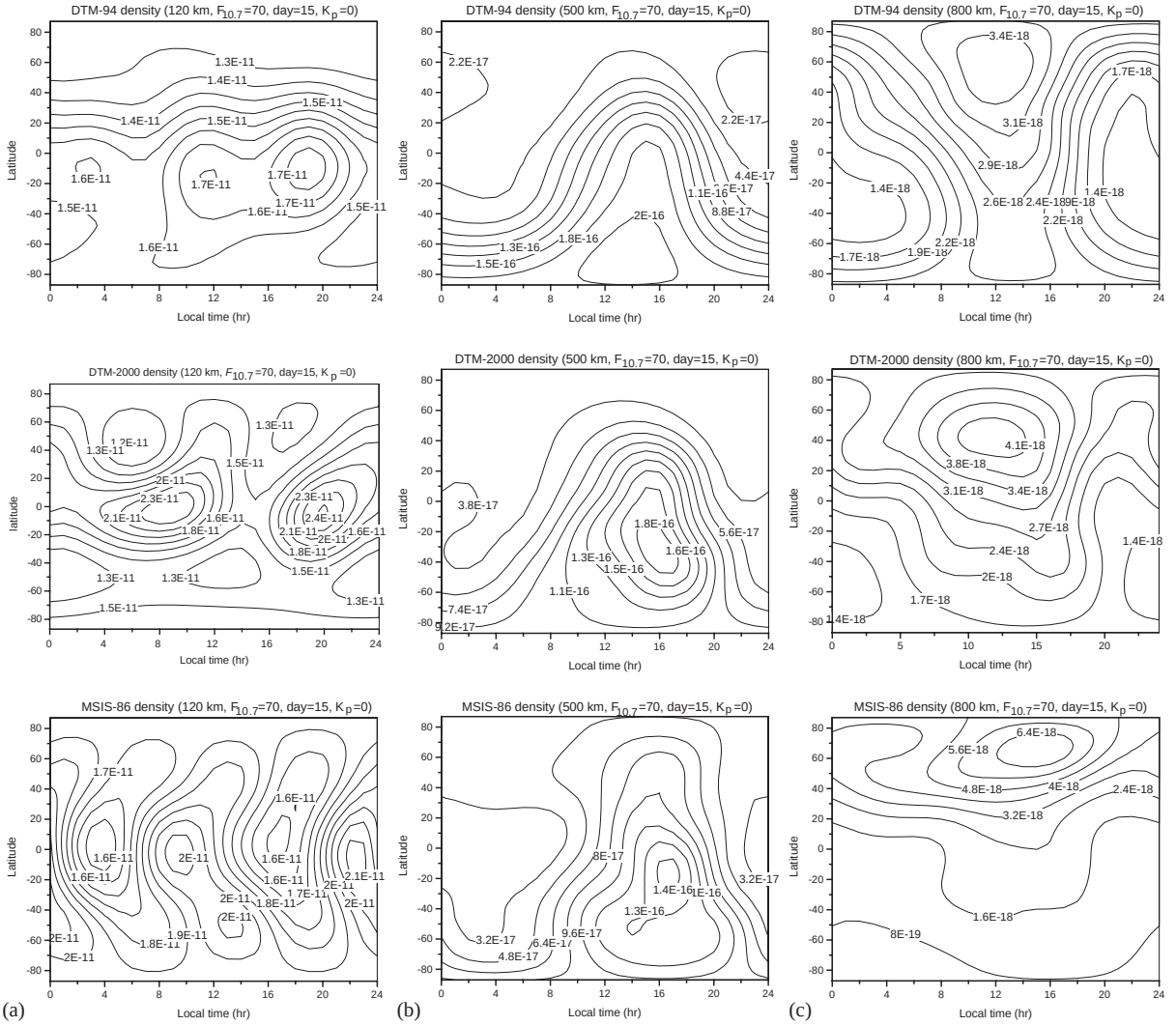

Fig. 9. Geographical distribution of density at 120 (a), 500 (b) and (c) 800 km, obtained with DTM-94, DTM-2000 and MSIS-86.

and the semi-annual variation is smaller than with the other two models.

A means to evaluate a density model performance consists in estimating and analysing the drag scale coefficients issued from orbit computation (see Section 2.6 and Marcos et al., 1993). If the density model is unbiased, the mean of the estimated drag scale factors is unity (the model density is then multiplied by 1, and thus unchanged). Tables 4 and 5 presents the POD results obtained with Starlette, Stella and GFZ-1 in the form of the mean and RMS about mean of the estimated drag scaling coefficients of several epochs, varying from 28 to 70 days (i.e. 4 and 10 orbital arcs, respectively, of 7 days in length) for Starlette and Stella, and 16 days (i.e. 4 orbital arcs of 4 days length) for GFZ-1. The Starlette orbital arcs in the period 10/03/1992 through 19/05/1992 were used to scale the DE-2 oxygen data set. The bias of DTM-2000 (the estimated multiplicative drag scaling coefficients are not unity on average) compared to those of DTM-94 and MSIS-86 under both low and high solar flux is significantly less: it ranges from 1% to 13% for DTM-2000, 2% to 30% for DTM-94 and 0% to 28% for MSIS-86. The only case in which MSIS-86 performs better than DTM-2000 is for GFZ-1, with a comparable mean value but a smaller RMS of the drag scale coefficients (0.12 compared to 0.14), and Starlette (4th frame) with a higher bias and equal RMS for DTM-2000 with respect to MSIS-86.

4.3. Helium modelling

As shown in Table 3, the helium modelling under low solar activity conditions (AE-E NACE data) is improved by 3% with respect to DTM-94, while under high solar activity

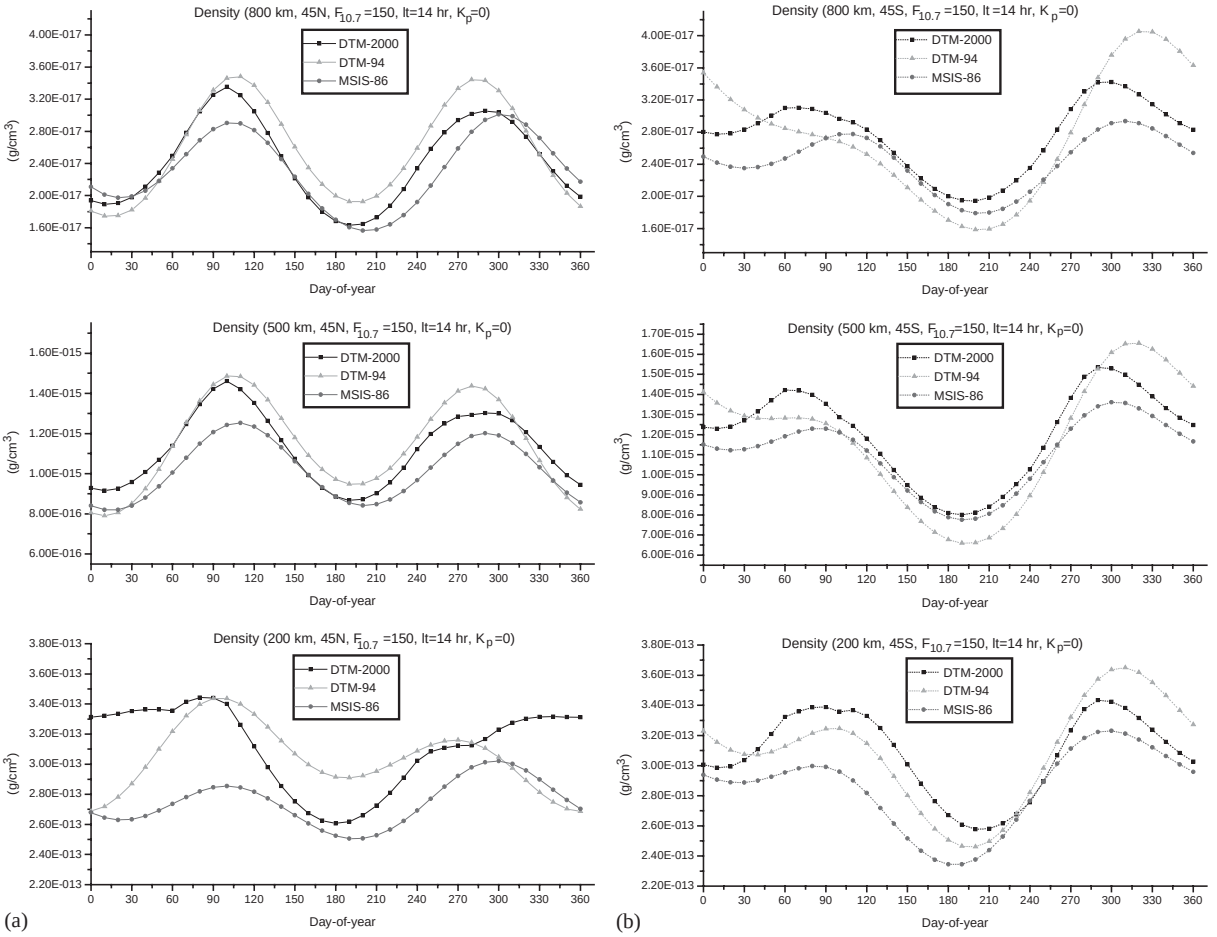

Fig. 10. Density as a function of day-of-year at 200, 500 and 800 km, obtained with DTM-2000, DTM-94 and MSIS-86, for 45°N (left column) and 45°S (right column).

Table 4
The calibration scale factors determined for the DE-2 NACS data

Data set	DTM-94	DTM-2000	MSIS-86
DE-2 NACS N_2	0.70 ± 0.26	0.68	0.60
DE-2 NACS O	0.91 ± 0.24	0.79	0.89
DE-2 NACS He	0.86 ± 0.28	0.63	0.86

the gain in precision is 1% (second frame). Table 3 shows that the mean of the AE-E helium residuals is 0.70 and that of DE-2 NACS helium is 0.63 with DTM-2000. The mean of the DE-2 helium residuals obtained with DTM-94 is 0.79. The smaller mean of the DTM-2000 residuals than those of DTM-94 is due to the 15% higher helium concentration at 120 km of the former model. DTM-2000 reproduces the DE-2 and AE-E data sets untrended from low to high solar activity. This is shown in Fig. 11, which equally shows the slightly trended results for DTM-94 and MSIS-86. The orbit tests under low solar activity shown in Table 5 (lines 1–5) represent the second way to evaluate model accuracy; and the smallest biases are obtained with DTM-2000. However, these results indicate a smaller residual than those obtained with DTM-94 and MSIS-86. This difference will be discussed in Section 4.7.

Further analysis revealed that both models produce large discontinuities when the residuals are binned as a function of month, but not for the same months: February and April for DTM-94, March for DTM-2000. For MSIS-86, it is the month of May that stands out. The gain in precision under low solar activity (AE-E NACE data) is mainly due to a better local time modelling. The helium modelling as a function of latitude and local time is given in Fig. 9 for DTM-2000, DTM-94 and MSIS-86 (altitude 800 km, flux = mean flux = 70, day-of-year = 180, $K_p = 0$), since under those conditions helium is the major constituent at 800 km. As expected the helium bulge is located on the high

Table 5
The mean and RMS of the estimated drag scale coefficients issued from precise Starlette (Sta), Stella (Ste) and GFZ-1 (GFZ) orbit computation, under low (L) or high (H) solar activity, using DTM-94, DTM-2000, or MSIS-86

	DTM-94	DTM-2000	MSIS-86
Sta (25/08/97–29/09/97) (L)	1.30; 0.14	1.00 0.09	1.28; 0.14
Sta (30/12/96–04/03/97) (L)	1.08; 0.09	1.02; 0.07	1.12; 0.22
Ste (30/12/96–04/03/97) (L)	1.13; 0.08	1.12; 0.09	1.11; 0.09
Sta (25/11/96–30/12/96) (L)	1.16; 0.16	1.12; 0.14	1.04; 0.14
Ste (01/03/96–04/05/96) (L)	1.04; 0.06	1.00; 0.06	1.03; 0.07
Sta (10/03/92–19/05/92) (H)	1.14; 0.16	0.99; 0.12	1.11; 0.19
Sta (07/01/92–04/02/92) (H)	1.23; 0.21	1.13; 0.13	1.12; 0.18
GFZ (01/06/96–17/06/96) (L)	0.98; 0.14	1.01; 0.14	1.00; 0.12

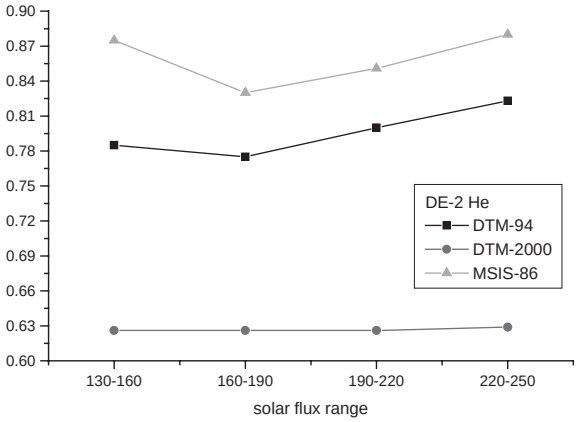

Fig. 11. Mean of the DE-2 helium residuals as a function of 81-day mean 10.7 cm solar flux.

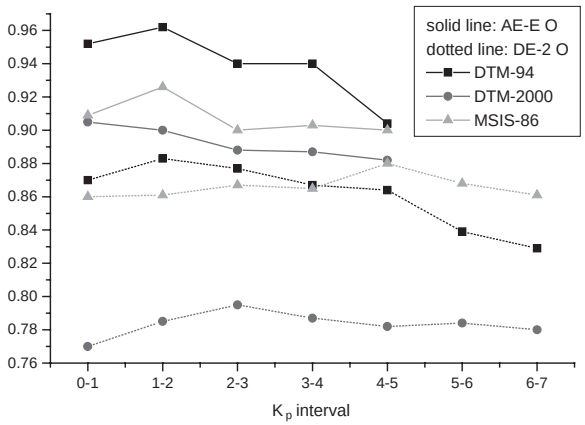

Fig. 12. Mean of the AE-E and DE-2 oxygen residuals as a function of geomagnetic activity.

latitude winter hemisphere. DTM-2000 is much closer to MSIS than DTM-94, and both agree in terms of maximum density.

While not detected, a possible source of error in the helium modelling may be due to an unmodelled component, hot oxygen (O^+). O^+ contributes significantly to the total density under the conditions low solar activity, summer, high latitude and altitude higher than 600 km (Keating et al., 1998), while densities derived from satellite drag under those conditions are attributed to helium.

4.4. Atomic oxygen modelling

Table 3 (third frame) shows that the larger improvement is obtained with respect to the DE-2 data, approximately 2.0% with respect to the two other models. A 0.7% higher precision is obtained with AE-E NACE with respect to DTM94, but an equivalent lower precision with respect to MSIS-86. The AE-C data are noisy, the instrumental precision being inadequate for the low partial densities as encountered under solar minimum conditions. Still, an improvement of 1.5% is achieved compared to DTM-94 (RMS of the residuals of 26.3 vs. 27.8% in Table 3), but it degrades by 1.1% with respect to MSIS-86. The improvement is mainly under high solar activity conditions, likely due to better data. The improvement is smaller under low solar activity conditions for two reasons: the Mg II index is not available, and secondly, the data sets contributing to the oxygen modelling have an adequate geographical coverage (DTM database and CACTUS), ensuring already accurate modelling in DTM-94. The smaller mean of the residuals obtained with DTM-2000 (0.79 vs. 0.87 with DTM-94 in Table 3) under high solar activity is due to a 10% higher atomic oxygen concentration at 120 km as well as a 15% stronger dependence on solar activity. This is due to the use of the Mg II index, which has a different signature than the solar radio flux during the DE-2 mission.

Binning of the data showed that DTM-2000 reproduces variations as a function of day-of-year and solar local time better than DTM-94 and MSIS-86 (not shown). Fig. 12 displays the residuals of the DE-2 and AE-E NACE oxygen data sets as a function of K_p. This figure shows a stable mean of the residuals of DTM-2000 and MSIS-86, and a weakly

drifting one for DTM-94 with increasing geomagnetic activity. The small value of the DTM-2000 residual, as already seen above, will be discussed in Section 4.7.

4.5. Molecular nitrogen modelling

The molecular nitrogen modelling is not improved under high solar activity (DE-2 data), but Table 3 (4th frame) shows that the AE-E NACE data fit better (bias and RMS smaller by 4% and 2%, respectively) with respect to DTM94, but has a lower precision with respect to MSIS-86 (24% versus 21.8%). Molecular nitrogen is by far the worst restituted major constituent for the three models with a global RMS of the residuals of up to 28%, as shown in Table 3. The DE-2 data could not be modelled with higher precision, even when they were fitted in absence of all other N_2-contributing data sets. Our interpretation of this result is that the DE-2 molecular nitrogen data are significantly affected by noise. The scale factors given by the three models for the DE-2 NACS data are small (0.56–0.68), while they are close to one for AE-NACE. This will be taken into account in the discussion of Section 4.7.

The binning as a function of latitude revealed large signature (mainly $P_{2,0}$) in the DE-2 residuals, which could not be corrected for without deteriorating the fit of the AE-E N_2, CACTUS and DTM database data sets. It was also not possible to accurately reproduce variations as a function of daily or mean solar activity. These results appear to incriminate the consistency and precision of the data set. The N_2 modelling under low solar activity improves by approximately 2% when compared to DTM-94. However, it is still 2% less precise than MSIS-86 which has a significantly better local time representation (not shown). The RMS is large for the AE-E residuals because the observations were taken under low solar activity where the instrumental sensitivity reaches its limit.

4.6. Modelling of molecular oxygen and hydrogen

Besides the major constituents already described above, molecular oxygen and hydrogen are represented in DTM-2000. Hydrogen becomes the major constituent above approximately 1400 km altitude when the solar activity is low. At that altitude (and higher) the atmospheric drag force is at least three orders of magnitude smaller compared to the radiation pressure forces acting on a satellite. It is therefore not necessary to model it with high accuracy for that application. The hydrogen representation in DTM-2000 remains as in DTM-94, which is to say, identical to MSIS-86.

For altitudes below 150 km this reasoning is not valid where molecular oxygen is concerned. At those altitudes, MSIS-86 (and also DTM-94) predicts a partial O_2 density that is up to 20% of the total density. Unfortunately, O_2 is always a minor constituent and can therefore not be deduced from satellite drag data. The spectrometers aboard the AE satellites measured O_2, but with low accuracy and small geographic coverage. Assimilation of those data was not successful and was abandoned. A second problem with the O_2 modelling is due to the assumption of diffusive equilibrium, which is not realistic (Aikin et al., 1993). However, the relative density variations described in Section 2.3 are implemented in DTM-2000. This is achieved through modification of the N_2 and O_2 constituent modelling.

4.7. Discussion of mass spectrometer results

The scale factors applied in this study to the DE-2 (Table 4) and AE-E mass spectrometer data are different from the ones used in the construction of MSIS-86 and DTM-94. This is in part due to the different approach that was used to determine them, which is based on the unbiased (i.e. unity) estimation of drag scale factors in the POD. Secondly, a different solar activity proxy is used in this study, the Mg II index. The mean solar activity is higher with Mg II than with $F_{10.7}$ over the DE-2 mission, and therefore not the same observations are used in the comparison to total density data or satellite drag data (from POD). The numerical conditions of the adjustment procedure of the model coefficients are thus also different.

The German CHAMP mission (Reigber et al., 1996) is expected to contribute significantly to upper atmosphere studies as will de discussed in Section 6. The satellite is in a circular, nearly polar orbit at 470 km altitude (initially) since July 2000. The CNES contribution to this mission consists of the STAR accelerometer, which provides non-gravitational acceleration measurements, from which the total atmospheric density can be extracted. A comparison of DTM-2000 to an independent total density data set derived from CHAMP/STAR accelerometer observations (Bruinsma and Biancale, 2001) demonstrated that, at least for atomic oxygen (i.e. the major constituent at the CHAMP altitude of 450 km), the small DE-2 scale factors applied in DTM-2000 are consistent. The data, spanning 6 weeks in September through October 2000, are reproduced 7% too large on average when the Mg II index is used (mean of the residuals: 0.93), and 10% too small when the solar radio flux is used. DTM-94 and MSIS-86 reproduce the data approximately 20% too small (mean of the residuals: 1.20). The CHAMP mission (Reigber et al., 1996) will be described in some more detail in Section 6.

5. Discussion

One of the reasons for the slow progress in thermosphere modelling is due to the data that we dispose of today. The last thermospheric satellite mission, DE-2, ended in 1983. MSIS-86, DTM-94 and DTM-2000 have therefore been constructed for a large part with the same data. However, these data do not provide adequate geographical coverage (altitude, latitude and solar local time), they are not representative of an entire solar cycle (low to high solar activity),

or they are affected by bias and/or noise. For example, the only consistent single-instrument data set that covers low to high solar activity is from the AE-E NATE instrument. But the geographical coverage of that data set is limited by the orbital inclination of AE-E: 20°. This means that the temperature variations at higher latitudes under low solar activities are not constrained by observation, which is imperative in empirical modelling. Similar shortcomings due to limited geographical coverage or mission duration affect all data sets. An important consequence of this is that the calibration (scale) factors of the DE-2 mass spectrometer cannot be well-determined by direct comparison with total density observations, but must be obtained through comparison with model results (DTM-94), or through simultaneous estimation of the model coefficients (MSIS-86) as well as POD results (DTM-2000).

The AE-E spectrometer data have an uncertainty of 20–40% under low solar activity, and data were eliminated due to partial pressures below instrument sensitivity. The DTM database resulted from semi-major axis decay determinations of over a hundred satellites, which ensures its adequate geographical and solar activity coverage. Due to the sparse tracking capability, the lesser accuracy of gravity field models as well as the less-complete radiation pressure modelling in the sixties and seventies, the instantaneous satellite position and velocity vectors could not be estimated accurately. To reduce random uncertainties, effects due to variable geomagnetic activity and geophysical noise (e.g. waves, winds, ..), the average orbit parameters over one to several days were estimated. This limits the accuracy of the database to the 5–15% stated in Table 1. Binning of the residuals of the DTM database and of the mass spectrometer data as a function of the model parameters revealed sudden spike-like steps (binning as a function of month) or offsets from one bin to the next (binning as a function of solar flux). These cannot be reproduced nor introduced by the DTM algorithm, but are most probably due to the non-homogeneous accuracy of the estimated orbit parameters, caused by different orbit configurations, satellite shapes, epochs and tracking coverage.

N_2 represents the least accurately restituted major constituent in DTM-94, MSIS-86 and DTM-2000. The DE-2 data appear to be inconsistent and less precise than the O and He measurements for reasons we ignore. The total density data sets provide too few observations in the 120–225 km altitude interval, where N_2 is the major constituent (approximately 75–50% of the predicted composition), and therefore cannot be used to estimate its variation. In the 120–130 km altitude interval, the DTM-94 predicted O_2 partial density (10–20% of the total composition) is larger than that of O. The DTM-2000 predictions are within 5–10% (larger) of DTM-94, and also within 5–10% (smaller) of MSIS-86. The two major constituents at 120 km (N_2 and O_2), constituting over 90% of the atmospheric composition, are thus not well observed. However, comparison to the AE-C MESA total density data learned that the DTM-2000 mean bias is approximately 5% in the 140–300 km altitude range under low solar activity.

The second reason for the slow progress in density modelling is due to the use of a solar activity indicator, $F_{10.7}$, that is not representative of atmospheric heating on time scales of the order of a few solar rotations. The contribution of the Mg II index to DTM-2000 is relatively small because at present only the DE-2 data are concurrent with the Mg II index, and so both Mg II and $F_{10.7}$ had to be used in the determination of its model coefficients. Assimilation of new observations, described in the next section, will increase the impact of the Mg II index.

The modelling algorithm constitutes the third limiting factor: it is designed to reproduce only stationary atmospheric conditions. Local effects, such as caused by gravity waves, cannot be reproduced and are therefore sources of geophysical noise in the modelling scheme. These waves, with horizontal scales of 10–1000 km, propagate upwards from the lower atmosphere. They are caused by the shearing instability of larger-scale flows, airflow over irregular and unevenly heated topography and variations in energetic particle precipitation. Analysis of Space Shuttle re-entry profiles showed amplitudes of the order of 10–20% for altitudes of 120–140 km (Fritts et al., 1993). Much larger amplitudes of up to 50% at 200 km altitude are reported in Marcos et al. (1993). The planetary geomagnetic activity index K_p is given every 3 h, but the storm onsets are much faster and so the used index may be inaccurate over part of the 3-h interval. It is equally only fully representative of geomagnetic activity for sub-auroral latitudes ($|35–60°|$) (Menviele and Berthelier, 1991).

Tests showed that a modelling precision of 11% for DE-2 oxygen at low latitudes (-30 to $30°$) is obtained. The current accuracy of the total density is approximately 19% (CACTUS and DTM database in Table 4). An accuracy of 15%, and probably 10% if a complete and consistent data set becomes available, is achievable with the empirical model algorithm in its present form, but has not yet been attained.

6. Future improvements

The upper atmosphere empirical modelling effort has presently reached a status quo due to the data problems discussed in the preceding section. The CHAMP nominal mission is scheduled for a 5-year operation, during which time the altitude will decrease to 250 km by natural decay or orbit manoeuvres. Total density data will be obtained with a single instrument during solar maximum (2000–2002) to nearly solar minimum (2005). The orbit provides an appropriate local time sampling for geophysical studies of 24 h approximately every 3 months. Moreover, these data will be processed using the Mg II index, which will decrease the RMS of the residuals. This was demonstrated with a STAR-derived 6-week density data set (Bruinsma and Biancale, 2001), which also showed the precision of

the derived densities at the few percent level. Finally, the CHAMP total density data will also enable the direct calibration of the DE-2 oxygen data set, and maybe the DE-2 molecular nitrogen data set as well, assuming a stationary atmosphere. The GRACE satellites (GRACE, 1998), launched in March 2002, are also equipped with accelerometers. Once these data are available, they can be processed similar to the CHAMP data in order to obtain total densities.

A second mission, TIMED (Thermosphere Ionosphere Mesosphere Energetics and Dynamics), is measuring temperature and wind at the lower model boundary during high solar activity (launched December 2001). This will improve the T_{120} and $\mathrm{d}T_{120}$ modelling which is now based for the largest part on data from only three incoherent scatter radars, and a dependency on solar flux may be determined. The relative density variations derived from the tidal winds may be used to determine a probable solar activity dependence. This mission is planned for 1 year, which makes the retrieval of annual variations delicate, and an extended mission would be necessary.

Further improvement could be expected by using sectorial geomagnetic planetary indices instead of K_p. Gravity wave activity has a large impact on the density structure of the upper atmosphere, but it cannot be modelled presently. A characteristic index could be useful to better understand the observed variations. A study of gravity wave interaction and propagation in the thermosphere, as well as the construction of an index, are therefore required. The CHAMP and GRACE accelerometers are sufficiently sensitive for this kind of analysis.

7. Conclusion

The latest version of DTM, DTM-2000, has been constructed using AE-C and AE-E data besides the data already assimilated in DTM-94. This allowed significant improvement of the temperature and helium modelling under low solar activity: the temperature bias of 3% has been corrected and the accuracy augmented by approximately 0.5%, while the helium modelling is approximately 3% more precise. The atomic oxygen modelling has been improved by 1–2%. Molecular nitrogen is predicted with the smallest precision of the major constituents, 24–28%. The total density is reproduced with an average bias of 1–5% depending on the altitude and solar activity.

The T_{120} and $\mathrm{d}T_{120}$ modelling constrains the lower model boundary which is now in accordance with tidal theory (semi-diurnal variation). The resulting density at 120 km, at least under low solar activity, agrees in amplitude and phase with the density variations derived from modelled tidal winds using WINDII observations. The density below 200 km, now better in accordance with tidal theory and observations under low solar activity, is predicted with a mean bias of approximately 5% and a 1σ uncertainty of 20% based on comparison to AE-C-MESA observations. At higher altitudes, the density modelling is unchanged despite the new temperature model.

The total and partial density data sets in particular present inconsistencies at the 5–15% level that are sometimes related to different phases of a mission (change of orbital altitude, for example) or to solar activity level. In addition, several partial density data sets suffer from calibration problems that are for the moment difficult to solve. Even when all data sets are used, the geographical and solar flux coverages are incomplete. Moreover, not all data sets are compatible; differences of 5–10% were found. Taking the instrumental precision into account as well, this all adds up to an uncertainty at the 10–30% level. The most important factor limiting empirical thermosphere modelling is that the available density, temperature and solar activity data are not adequate or incomplete. It has been demonstrated that the Mg II index is more representative of solar EUV activity than $F_{10.7}$ is, but it is not available on a continuous basis.

The DTM algorithm is not designed to model local variations such as gravity waves, which are considered as noise in the observations. The fast variations due to solar or geomagnetic activity cannot be modelled using the proxy-indicators Mg II, $F_{10.7}$ and K_p because of their limited temporal resolution.

Acknowledgements

This study was supported by the Centre National d'Etudes Spatiales (CNES). The authors acknowledge the CEDAR database (http://cedarweb.hao.ucar.edu). We thank C. Lathuillère for the EISCAT data. We thank F.A. Marcos and an anonymous referee for reviewing this paper.

References

Aikin, A.C., Hedin, A.E., Kendig, D.J., Drake, S., 1993. Thermospheric molecular oxygen measurements using the ultraviolet spectrometer on the Solar Maximum Mission spacecraft. Journal of Geophysical Research 98, 17607–17613.

Alcaydé, D., Bauer, P., Fontanari, J., 1974. Long-term variations of thermospheric temperature and composition. Journal of Geophysical Research 79, 629–637.

Banks, P.M., Kockarts, G., 1973. Aeronomy, Part B. Academic Press, New York, London.

Barlier, F., Berger, C., Falin, J.L., Kockarts, G., Thuillier, G., 1978. A thermospheric model based on satellite drag data. Annales de Geophysique 34, 9–24.

Bates, D.R., 1959. Some problems concerning the terrestrial atmosphere above about the 100-km level. Proceedings of the Royal Society A. 253, 451–462.

Berger, C., Biancale, R., Ill, M., Barlier, F., 1998. Improvement of the empirical thermospheric model DTM: DTM-94- comparative review on various temporal variations and prospects in space geodesy applications. Journal of Geodesy 72, 161–178.

Bruinsma, S.L., Biancale, R., 2001. STAR accelerometer data processing and results: Part II. AAS paper 01-333.

Bruinsma, S., Vial, F., Thuillier, G., 2002. Relative density variations at 120 km derived from tidal wind observations made by the UARS/WINDII instrument. Journal of Atmospheric and Solar-Terrestrial Physics 64, 13–20.

Carignan, G.R., Block, B.P., Maurer, J.C., Hedin, A.E., Reber, C.A., Spencer, N.W., 1981. The neutral mass spectrometer on Dynamics Explorer. Space Science Instruments 5, 429–441.

Cebula, R.P., DeLand, M.T., Hilsenrath, E., 1998. NOAA-11 Solar Backscattered Ultraviolet, model 2 (SBUV/2) instrument solar spectral irradiance measurements in 1989–1994 1. Observations and long-term calibration. Journal of Geophysical Research 103, 16235–16249.

Cook, G.E., 1965. Satellite drag coefficients. Planetary and Space Science 13, 929–946.

Fesen, C.G., Roble, R.G., Ridley, E.C., 1991. Thermospheric tides at equinox: simulations with coupled composition and auroral forcing, 2, semidiurnal component. Journal of Geophysical Research 96, 3663–3677.

Fritts, D.C., Wang, D.-Y., Blanchard, R.C., 1993. Gravity wave and tidal structures between 60 and 140 km inferred from Space Shuttle reentry data. Journal of the Atmospheric Science 50, 837–849.

Gaposhkin, E.M., Coster, A.J., 1994. Evaluation of thermospheric models and the precipitation index for satellite drag. Advances in Space Research 10, (3)303–(3)309.

GRACE, 1998. Gravity recovery and climate experiment: science and mission requirements document, revision A. JPLD-15 928.

Hagan, M.E., Forbes, J.M., Vial, F., 1995. On modeling migrating diurnal tides. Geophysical Research Letters 22, 893–896.

Heath, D.F., Schlesinger, B.M., 1986. The Mg 280 nm doublet as a monitor of changes in solar ultraviolet irradiance. Journal of Geophysical Research 91, 8672–8682.

Hedin, A.E., 1984. Correlations between thermospheric density and temperature, solar EUV flux, and 10.7-cm flux variations. Journal of Geophysical Research 89, 9828–9834.

Hedin, A.E., 1987. MSIS-86 thermospheric model. Journal of Geophysical Research 92, 4649–4662.

Hedin, A.E., 1989. Hot oxygen geocorona as inferred from neutral exospheric models and mass spectrometer measurements. Journal of Geophysical Research 94, 5523–5529.

Keating, G.M., Leary, J.C., Green, B.D., Uy, O.M., Benson, R.C., Erlandson, R.E., Phillips, T.E., Lesho, J.C., Boies, M.T., 1998. Neutral and ion drag effects near the exobase: MSX satellite measurements of He and O^+. In: Hoots, F., Kaufman, B., Cefola, P., Spencer, D. (Eds.), Astrodynamics 1997, Advances in Astronautical Science Part 1. American Astronautical Society San Diego, pp. 549–556.

Marcos, F.A., Baker, C.R., Bass, J.N., Killeen, T.L., Roble, R.G., 1993. Satellite drag models: current status and prospects. Paper AAS 93-621.

McLandress, C., Shepherd, G.G., Solheim, B., 1996. Satellite observations of thermospheric tides: results from the Wind imaging Interferometer on UARS. Journal of Geophysical Research 101 (D2), 4093–4114.

Menviele, M., Berthelier, A., 1991. The K-derived planetary indices: description and availability. Reviews of Geophysics 29, 415–432.

Nier, A.O., Potter, W.E., Hickman, D.R., Mauersberger, K., 1973. The open-source neutral-mass spectrometer on Atmosphere Explorer-C, -D, -E. Radio Science 8, 271–276.

Pelz, D.T., Reber, C.A., Hedin, A.E., Carignan, G.C., 1973. A neutral-atmosphere composition experiment for the Atmosphere Explorer-C, -D, -E. Radio Science 8, 277–283.

Reigber, Ch., Bock, R., Förste, Ch., Grunwaldt, L., Jakowski, N., Lühr, H., Schwintzer, P., Tilgner, C., 1996. CHAMP Phase B executive summary. Scientific Technical Report STR96/13, GeoForschungsZentrum Potsdam, Germany.

Shepherd, G.G., et al., 1993. WINDII, the Wind Imaging Interferometer on the Upper Atmosphere Research Satellite. Journal of Geophysical Research 98, 10 725–10 750.

Spencer, N.W., Niemann, H.B., Carignan, G.R., 1973. The neutral-atmosphere temperature instrument. Radio Science 8, 284–296.

Spencer, N.W., Wharton, L.E., Niemann, H.B., Hedin, A.E., Carignan, G.R., Maurer, J.C., 1981. The Dynamics Explorer wind and temperature spectrometer. Space Science Instrument 5, 417–428.

Thuillier, G., Bruinsma, S., 2001. The Mg II index for upper atmosphere modelling. Annales de Geophysique 19, 219–228.

Thuillier, G., Falin, J.L., Barlier, F., 1977. Global experimental model of the exospheric temperature using optical and incoherent scatter measurements. Journal of Atmospheric and Terrestrial Physics 39, 1195–1202.

Villain, J.P., 1980. Traitement des données brutes de l'accéléromètre CACTUS. Etude des perturbations de moyenne échelle de la densité thermosphérique. Annales de Geophysique 36, 41–49.